Supporting information for "Hierarchical anti-reflective laser-induced periodic surface structures on amorphous Si films via ultrafast laser nanotexturing."

Aleksandr Dostovalov[1,*], Kirill Bronnikov[1,2], Victor Korolkov[1], Sergey Babin[1], Eugeny Mitsai[3], Aleksandr Mironenko[4], Michail Tutov[5], Dongshi Zhang[6,7], Koji Sugioka[6], Jovan Maksimovic[8], Tomas Katkus[8], Saulius Juodkazis[8,9], Alexey Zhizhchenko[3], Aleksandr Kuchmizhak[3,*]

[1] *Institute of Automation and Electrometry of the SB RAS, 1 Acad. Koptyug Ave., 630090 Novosibirsk, Russia*

[2] *Novosibirsk State University, 2 Pirogova St., 630090 Novosibirsk, Russia*

[3] *Institute of Automation and Control Processes, Far Eastern Branch, Russian Academy of Sciences, Vladivostok 690041, Russia*

[4] *Institute of Chemistry, Vladivostok 690090, Russia*

[5] *Far Eastern Federal University, Vladivostok 690090, Russia*

[6] *RIKEN Center for Advanced Photonics, 2-1 Hirosawa, Wako, Saitama 351-0198, Japan*

[7] *Shanghai Key laboratory of Materials Laser Processing and Modification, School of Materials Science and Engineering, Shanghai Jiao Tong University, Shanghai 200240, China*

[8] *Swinburne University of Technology, John st., Hawthorn 3122, Victoria, Australia*

[9] *World Research Hub Initiative (WRHI), School of Materials and Chemical Technology, Tokyo Institute of Technology, 2-12-1, Ookayama, Meguro-ku, Tokyo 152-8550, Japan*

*Corresponding author
Email address:* alex.iacp.dvo@mail.ru (Aleksandr Kuchmizhak[3,*])

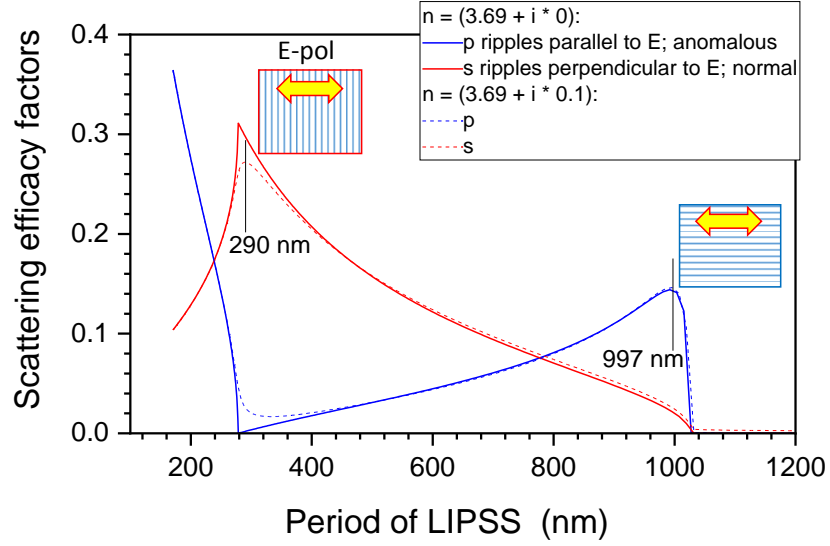## 1. LIPSS periods predicted by Sipe and van Driel model.

Figure 1: Normal and anomalous LIPSS periods for Si of refractive index $n = 3.69$ (at $\lambda = 1026$ nm) and with absorption $n = 3.69 + i \times 0.1$ calculated for s- and p-polarized irradiation according to Sipe and van Driel model. Explicit formulae is given in [H. Iwase, et.al. Opt. Express 17,4388 (2009)]. The scattering efficacy factor calculated by the model correlates with surface LIPSS patterns. For the normal incidence s- and p-pol. are same and the two cases represents two possibilities for ripples (LIPSS) to be aligned to the polarisation of E-field (anomalous ripples) and perpendicular (normal) as schematically shown by thumbnail insets. The period of normal ripples is expected as $\Lambda_n \approx \lambda/n$ and the anomalous $\Lambda_a \approx \lambda$ at the peak efficacy factors, respectively.
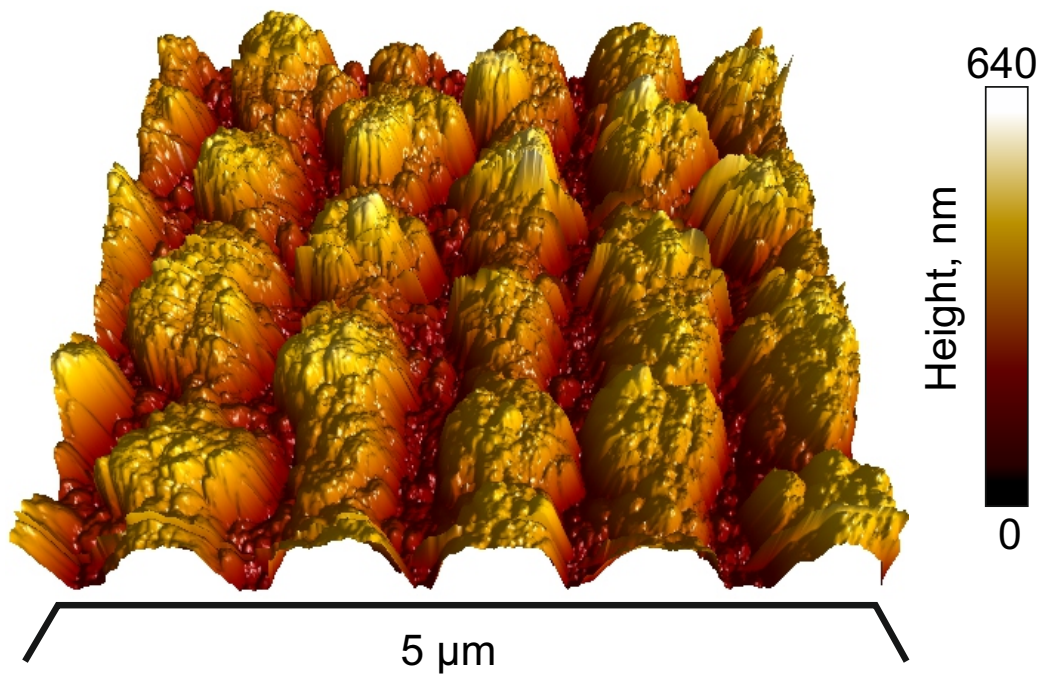
Figure 2: AFM image of LIPSS morphology (E= 1.5 μJ, V=3 μm/s) showing the maximal height of conical-shaped structures around 640 nm.
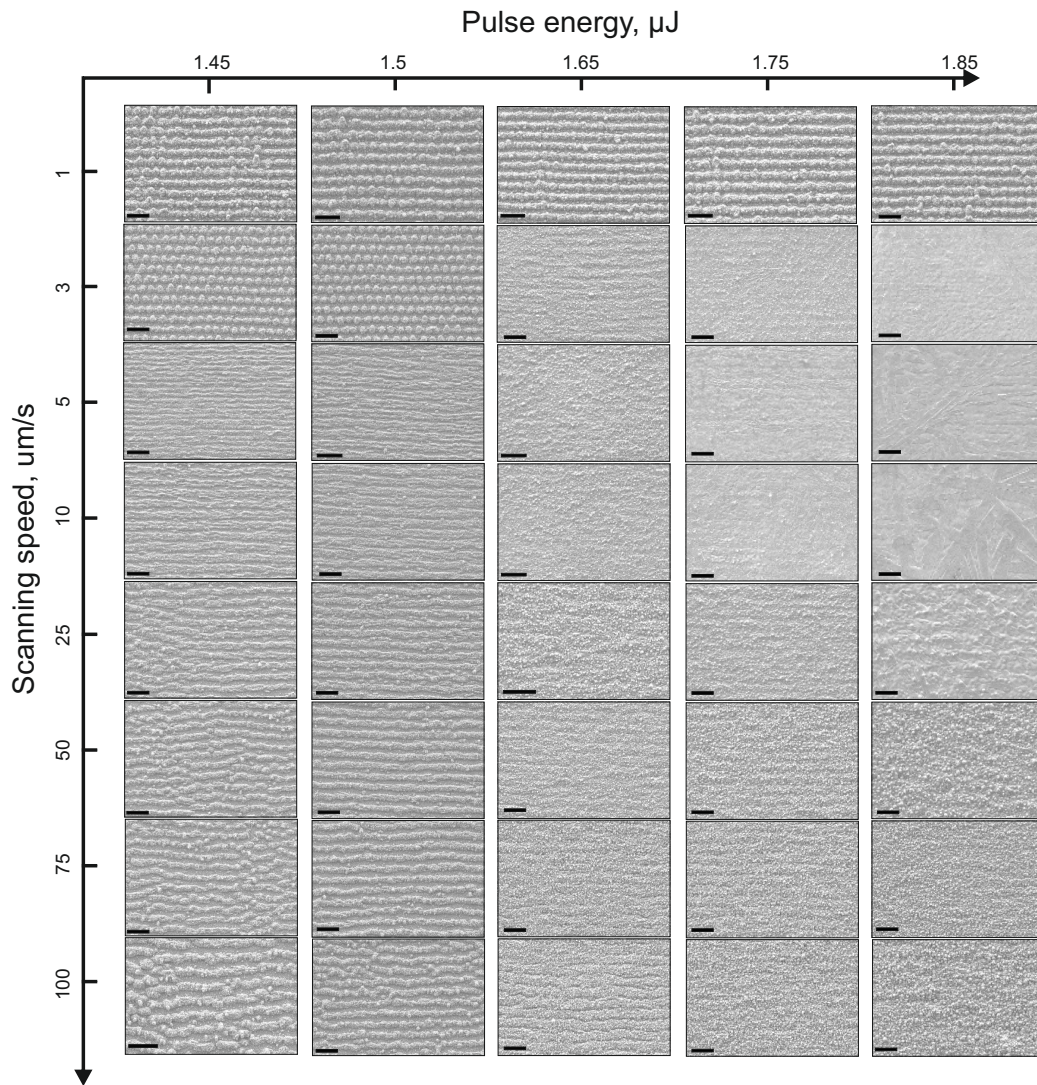
2. AFM analysis of LIPSS.

Figure 3: Diversity of the LIPSS morphologies is illustrated by series of top-view SEM images of LIPSS produced on 360-nm thick glass-supported a-Si film at variable pulse energies (1.45 - 1.85 μJ) and scanning speeds (1 - 100 μm/s).

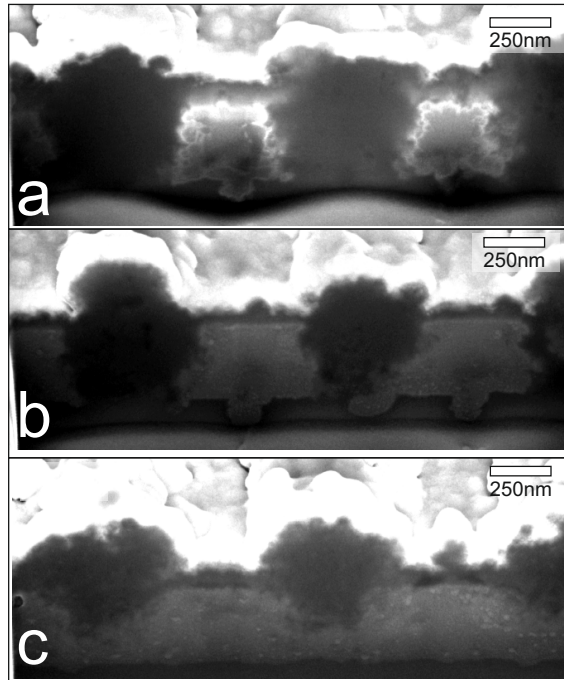## 3. Variation of LIPSS morphology versus laser processing parameters.

Figure 4: (a-c) True-color SEM images of FIB cross-section cuts of LIPSS fabricated on the a-Si film surface at various scanning speeds V of 1 μm/s (a), 3 μm/s (b), and 50 μm/s (c).)

4. True-color SEM contrast of FIB cross-section cut images.
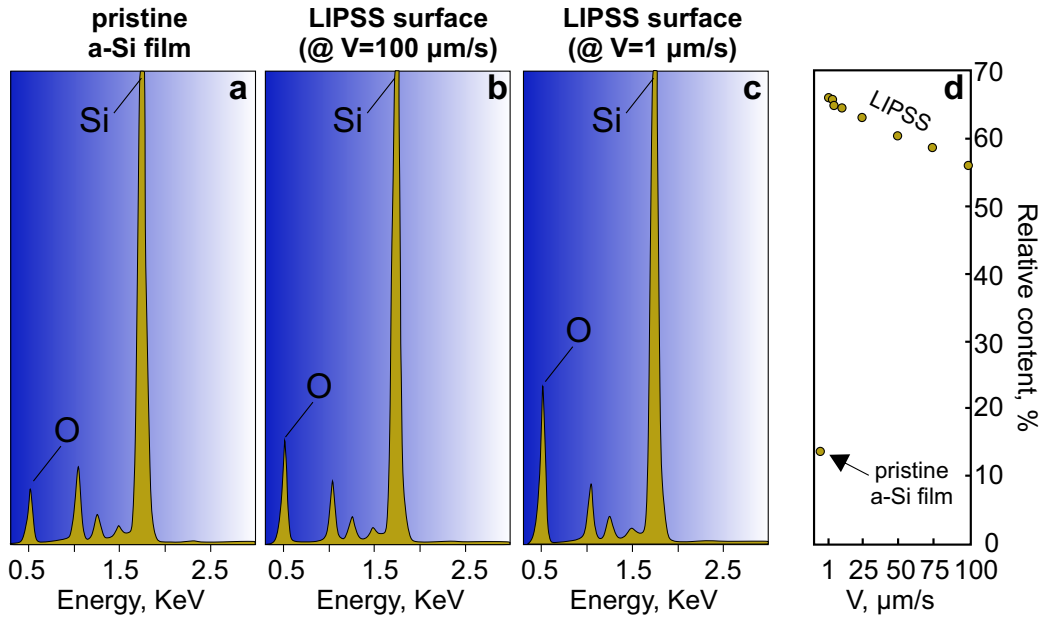
Figure 5: (a-c) Comparative EDX spectra of pristine a-Si film (a), LIPSSs produced at V=100 (b) and 1 μm/s (c) at E=1.5 μJ. (d) Relative content of oxygen calculated from EDX spectra versus the scanning speed V for LIPSSs at E=1.5 μJ. Relative content of oxygen obtained from EDX spectra of a-Si film ($\approx$14 %) is provided as reference. Each dot is the average of at least 30 similar spectra.

5. EDX analysis

Here, to confirm the increasing amount of oxygen in laser-processed areas we analyzed their chemical composition with energy-dispersive X-ray spectroscopy modality (Oxford Instruments, X-max) of the scanning electron microscope (Carl Zeiss, Ultra55+). For all measurements, the acceleration voltage and signal acquisition area was fixed at 20 kV and 50 μm^2, respectively. Relative content of oxygen measured in the pristine a-Si film ($\approx$14 %) was used as reference. Representative EDX spectra of pristine a-Si film as well as LIPSS produced at printing speed of V=1 and 100 μm/s are provided in Fig. S3(a-c). Fig. S3(d) summarizes the relative content of oxygen calculated from LIPSS produced at various scanning speed V.

6

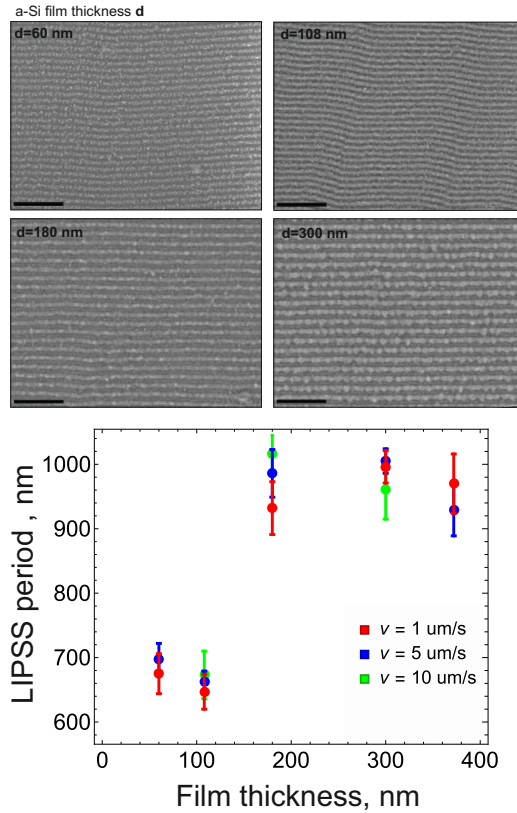Figure 6: Top-view SEM images of near-wavelength LIPSS formed on a-Si film at fixed pulse energy of 1.45 μJ and scanning speed of 3 μm/s and different a-Si film thickness d: 60 nm, 108 nm, 180 nm and 300 nm. (Bottom) Dependence of LIPSS period on Si film thickness measured for surface morphologies produced at scanning speeds V= 1, 5 and 10 μm/s.)

6. LIPSS period versus a-Si film thickness

To illustrate the step-like decrease of the near-wavelength period with a-Si film thickness, we carried out series of experiments. The a-Si films of variable thickness d ranging from 60 to 360 nm were deposited using magnetron sputtering under identical conditions at constant evaporation speed. LIPSS were fabricated under identical conditions at fixed pulse energy E=1.45 μJ and variable scanning speed V. Morphology of the produced LIPSS was further analyzed with SEM imaging allowing to identify LIPSS period summarized in Fig. S4(bottom) as a function of film thickness d.

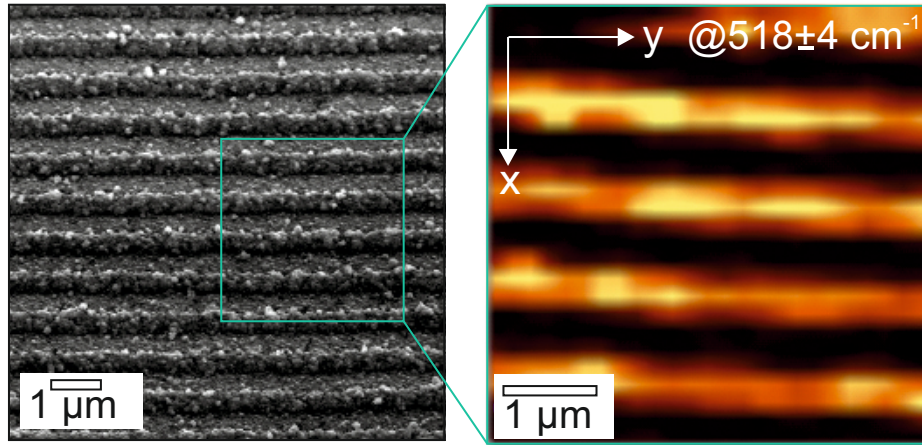Figure 7: Correlated SEM and Raman (@518±4 cm^{-1}) images of the LIPSS surface produced on 180-nm thick a-Si film at V=3 μm/s and E=1.5 μJ.)

7. Composition of LIPSS produced on the surface of 180-nm thick a-Si film.

In this section we show that LIPSS produced on the surface of twice thinner a-Si film (d=180 nm) preserve similar homogeneity and periodicity around 980 nm, while Raman mapping indicates similar structural and chemical composition - nc-Si pillars arranged parallel to the LIPSS orientation. This provide the way to tailor the height of the nc-Si pillars, which is obviously limited by the initial a-Si film thickness.
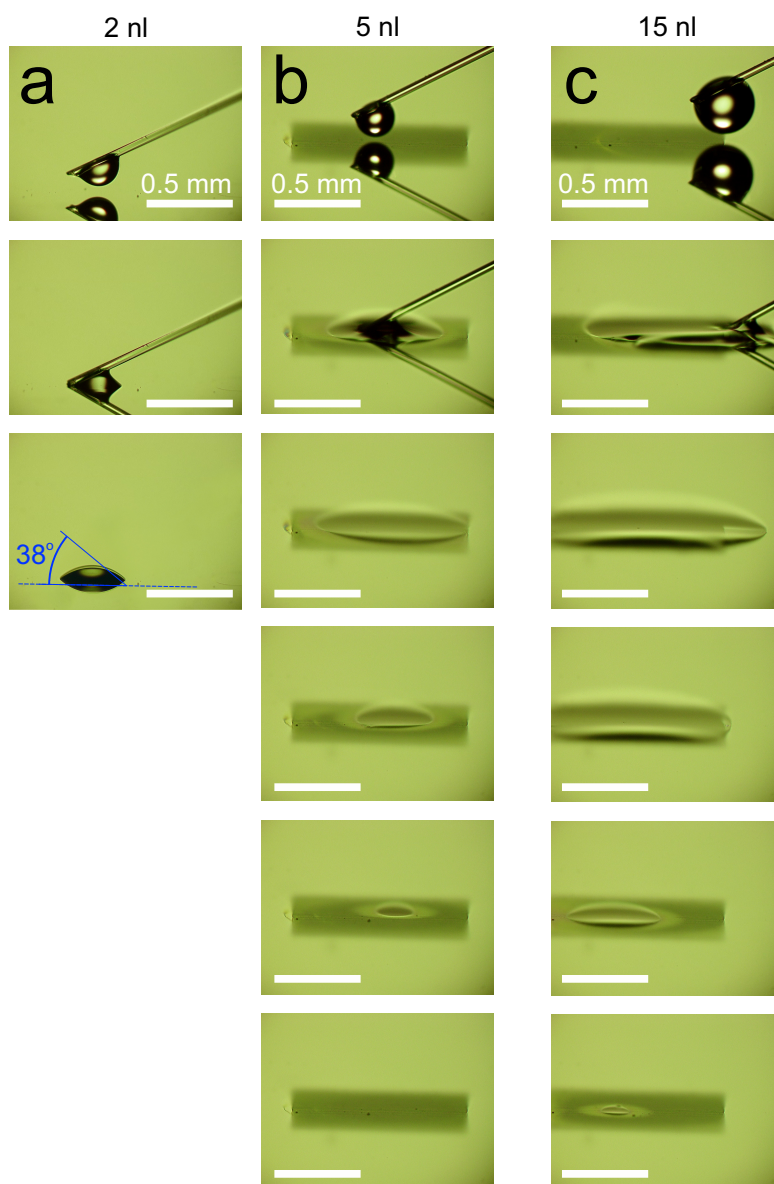
Figure 8: Optical photographs showing the deposition and spreading of the water droplets on a surface of pristine a-Si film (a), onto the 3D conical-shaped LIPSS at the center of patterned area (b), onto the boundary between similar LIPSS area and pristine a-Si film (c).)

8. Wetting properties of LIPSS.

In this section, we highlight good wetting properties of LIPSS that facilitate analyte deposition in sensing experiments. Series of optical photographs

9

indicates that the contact angle for a nL-volume water droplet reduces from 38° for pristine as-Si film to almost zero for LIPSS showing their good super-hydrophilic properties (Fig. S7(a,b)). Upon its contact with the LIPSS, the water droplet promptly spreads over the texture surface, and does not move beyond its borders. Being deposited near the boundary between LIPSSs and pristine a-Si (Fig. S7(c)), the capillary forces push the liquid towards the textured surface (even the part situated on the smooth a-Si), where the liquid finally evaporates providing analyte pre-concentration. Noteworthy, the left-side LIPSSs boundary is not shown owing to limited field of view of the optical system that was shifted to the right to show the liquid behavior on the right-side boundary.
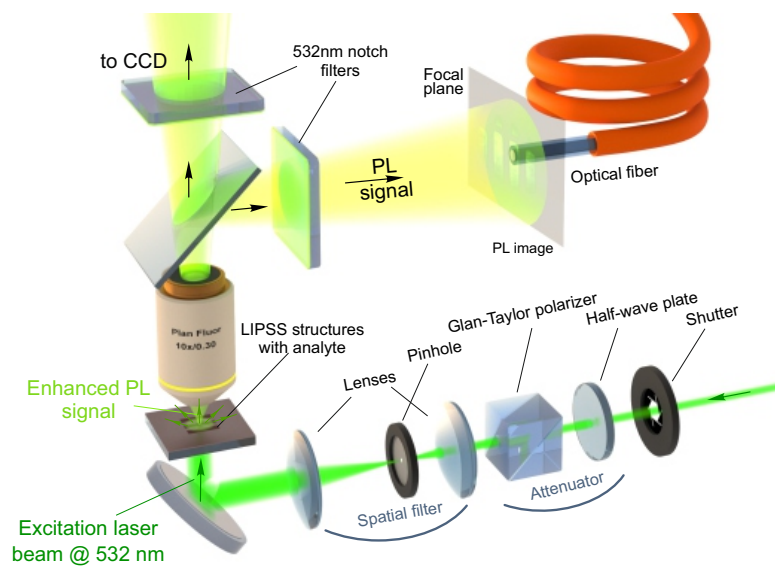
Figure 9: Schematic of the experimental setup used to assess applicability of LIPSS as SEF-based sensor of [Au^{3+}] ions.
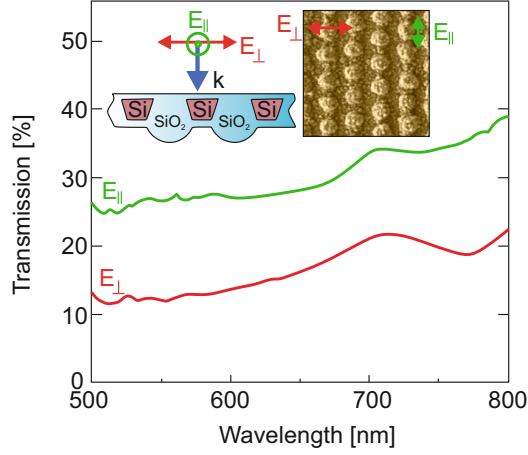
9. Experimental setup for SEF sensing experiments.

48

11

Figure 10: Difference of visible-range transmission through the 3D conical-shaped LIPSS (V=3 μm/s, E=1.5 μJ) for white light polarized either parallel (green) or perpendicular (red) to the LIPSS orientation. Top insets schematically illustrate excitation conditions as well as provide reference top-view SEM image of the tested LIPSS.)

10. Polarization-resolved transmission of 3D conical-shaped LIPSS.

Laser sources generating linearly polarized radiation are typically used for sensing experiments. In our sensing experiments shown in this paper, LIPSS morphologies represent periodical arrangement of nc-Si pillars capped with 3D SiO_2 protrusions were used. As any type of the grating, our textures are expected to have anisotropy of the optical properties, which means that the polarization direction of the pump laser radiation in sensing experiments should be properly adjusted to ensure maximal performance. To illustrate this feature, here we measure visible-range FTIR transmission thought the LIPSS (similar to those used for sensing experiments) probed with broadband visible light radiation polarized either parallel (green) or perpendicular (red) to the LIPSS orientation (Fig. S5). These measurements showed decreased transmission for light polarized perpendicular to nc-Si pillars orientation. Noteworthy, the reflection coefficient for both polarization orientations remained almost the same. Unfortunately, experimental limitations of the optical setup do not allow us to probe in a similar way near-IR part of the spectrum, where the anisotropy of optical properties is expected to be promoted by the LIPSS periodicity, which will be the subject of our further studies.

12